Nature-Inspired Halide Perovskite Breath Figures

Unleashing Enhanced Light-Matter Interaction

Sarkar, Prakash; Maitra, Tamaghna; Hossain, Mozakkar; Murugasenapathi, N. K.; Chirumamilla, Manohar; Palanisamy, Tamilarasan; Rao, K. D.M.

Published in:
Advanced Optical Materials

DOI (link to publication from Publisher):
10.1002/adom.202400353

Publication date:
2024

Document Version
Accepted author manuscript, peer reviewed version

Nature-Inspired Halide Perovskite Breath Figures: Unleashing Enhanced Light-Matter Interaction

*Prakash Sarkar, Tamaghna Maitra, Mozakkar Hossain, N. K. Murugasenapathi, Manohar Chirumamilla, Tamilarasan Palanisamy, K. D. M. Rao**

P. Sarkar, T. Maitra, M. Hosain, K. D. M. Rao
School of Applied & Interdisciplinary Sciences, Indian Association for the Cultivation of Science, Jadavpur, Kolkata 700032, India
Technical Research Centre, Indian Association for the Cultivation of Science, Jadavpur, Kolkata 700032, India
N. K. Murugasenapathi, T. Palanisamy
Electrodics and Electrocatalysis Division (EEC), CSIR-Central Electrochemical Research Institute (CECRI), Karaikudi 630003 Tamil Nadu, India;
Academy of Scientific and Innovative Research (AcSIR), Ghaziabad 201 002, India

Manohar Chirumamilla
Department of Materials and Production, Aalborg University, Skjernvej 4A, Aalborg 9220, Denmark
Institute of Optical and Electronic Materials, Hamburg University of Technology, Eissendorfer Strasse 38, Hamburg 21073, Germany

Abstract

Halide perovskites offer a transformative potential for optoelectronics through tailoring the light-matter interactions at the nanoscale. However, their susceptibility to environmental factors and limited compatibility with standard lithography techniques present significant challenges in precise nanopatterning. This work unveils a nature-inspired breath figures (BFs) approach to pattern halide perovskites and enhancing their optoelectronic performance. The fabrication of BFs based on BiI_3 allows for changes in nanopore size (ranging from 247 to 423 nm) and their distribution. Subsequently, these BiI_3 BFs are transformed into hybrid halide $MA_3Bi_2I_9$ BFs using a vapor-assisted technique while retaining the nanoporous topology of the BiI_3 structure. The resultant $MA_3Bi_2I_9$ BFs show significantly enhanced light absorption compared to conventional thin films, attributed to the increased extinction and lower refractive index. The optoelectronic performance of the $MA_3Bi_2I_9$ BFs is showcased by constructing a photodetector, which exhibits three orders of magnitude higher responsivity and detectivity, up to 1 A/W and 1.3×10^{12} Jones, respectively, outperforming the photodetectors based on solution-processed $A_3B_2I_9$ halide perovskite thin films. The BFs method provides flexibility in tuning nanoscale morphology, showcasing its potential in advancing lead-free optoelectronics and paving the way for next-generation optoelectronic devices.

Keywords: Breath Figures, Nanopores, Metal Halides, Halide Perovskites, Photodetector, Light-Matter Interaction

1. Introduction

Over the past two decades, the concept of breath figures (BFs) [1,2] has developed into a versatile and eco-friendly approach for fabricating self-assembled mesoporous polymer structures, with applications spanning from optoelectronics and biosensors to energy storage devices. [3–7] This method, influenced by the natural process where water vapor condenses on cold surfaces under humid conditions, mirroring the way how fog appears on windows after exhalation, forms

the foundation principle of the BFs approach. [8,9] BFs mimic this natural phenomenon where the rapid cooling of solvents leads to water droplet condensation, resulting in the organized self-assembly of polymers into mesoporous structures with precise control over topology.[9] This approach has progressed from small-scale lab experiments to large-scale industrial uses, offering a simpler alternative to complex lithography methods that often require hazardous chemicals.[10] However, despite its effectiveness with organic materials,[11] adapting BFs to inorganic materials, particularly halide perovskites, presents unique challenges. The volatile solvents in BFs often interact poorly with metal halides, limiting the solvent evaporation rate and the self-assembly process.[9,12,13] Additionally, the tendency of metal halides to crystallize and aggregate can disrupt the formation of uniform patterns and hinder self-assembly.[14,15] Furthermore, the potential for unwanted chemical reactions or phase transformations during solvent evaporation can obscure the process.[15,16] Despite the inherent complexities of these materials, the successful optoelectronic applications[17–20] of BFs to certain metal halides can be achieved by selecting appropriate solvents and modifying the process conditions.

The BFs approach, inspired by the natural process of solvent evaporation and self-assembly, provides a cost-effective, scalable, and precise way to fabricate polymer mesoporous structures. The BFs allow for controlling vital structural features like pore size (which can range from micro to nanoscale) and pore spacing, density, and orientation. Such versatility makes the BFs approach highly adaptable for various applications, [11,21] utilizing nature-inspired techniques to craft cutting-edge optoelectronic devices. In this context, polymer BFs serve as sacrificial templates for fabricating inverse opal structures using materials like ZnO, CdS QDs, and TiO_2.[22–24] The resulting nanoporous structures benefit from the high surface area-to-volume ratio of BFs, enabling significant light scattering and trapping within the active materials. This effect is

facilitated by multiple internal reflections, thereby increasing photon absorption and extending the path length of light within the structures. [11,25]

Bismuth (III)-based $MA_3Bi_2I_9$ has recently gained attention as a promising material, primarily due to its remarkable intrinsic stability attributed to the stereochemically active lone pair on Bi^{3+}.[26,27] This lone pair is crucial in inhibiting halide ion migration and preventing decomposition.[28] However, despite these stability advantages, $MA_3Bi_2I_9$ faces challenges with optoelectronic performance, primarily due to its inherent 0D crystal structure and high exciton binding energy (E_b). The 0D nature of the structure limits charge carrier (e-h) diffusion and transport, which in turn affects device efficiency by limiting exciton dissociation and increasing recombination losses.[29] To overcome these limitations, we introduce nanoporous structures into $MA_3Bi_2I_9$ through the bottom-up BFs method. This innovative strategy aims to improve optoelectronic performance through a multifaceted approach: (1) Amplified light-matter interaction: Light absorption efficiency can be maximized by increasing the surface area with a nanoporous network, leading to enhanced photocurrent generation. (2) Enhanced charge carrier generation: The nanoporous structure significantly increases e-h pair generation attributed to enhanced electric fields.[30] By effectively mitigating the intrinsic limitations of $MA_3Bi_2I_9$, the integration of nanoporous structures signifies a transformative step, unlocking the true potential of $MA_3Bi_2I_9$ in high-performance light-harvesting devices.

This work introduces a novel technique for fabricating nanoporous thin films of halide perovskites inspired by the BFs phenomenon. Initially, BiI_3 BFs are fabricated by spin-coating a precursor in tetrahydrofuran (THF) onto a glass substrate under specific humidity conditions. BiI_3 BFs with tunable nanopore radii (ranging from 247 to 423 nm) were obtained by modifying the precursor concentration and the spin-coating process parameters. The BiI_3 BFs, unlike their more

orderly structured polymer counterparts, exhibit polydispersity and a higher degree of conformational entropy in the nanopores, owing to the fusion and coagulation of water droplets during BF formation. The BiI_3 BFs serve as a template for transforming into hybrid halide $MA_3Bi_2I_9$ BFs. Finite difference time domain (FDTD) simulations demonstrate how the electric field distribution within $MA_3Bi_2I_9$ BFs varies with wavelength, highlighting the impact of their unique geometric structures on enhanced light harvesting. These optical properties of $MA_3Bi_2I_9$ BFs include increased light absorption and a lower refractive index. A photodetector incorporating $MA_3Bi_2I_9$ BFs is fabricated to evaluate optoelectronic performance, outperforming conventional thin-film photodetectors due to improved light-matter interactions and enhanced light harvesting properties. These improvements are attributed to the random nanoporous thin film structure originating from the BiI_3 BFs template.

2. Experimental Section

Materials: BiI_3 is acquired from Sigma Aldrich, and methylammonium iodide (MAI) is sourced from Lumtec, Taiwan. Tetrahydrofuran (THF) with 99% purity is obtained from Merck EMPLURA.

Fabrication of BiI_3 and $MA_3Bi_2I_9$ BFs: To ensure the fabrication of films without pinholes, the THF solvent is subjected to double filtration using Whatman filter paper with a pore size of 0.5 µm. For the fabrication of BiI_3 BFs, a BiI_3 solution with a concentration of 84.79 mM is prepared by dissolving 150 mg of BiI_3 in 3 ml of THF, followed by sonicating for 30 minutes at a temperature < 35 °C. Different concentrations of the BiI_3 precursor solutions, ranging from 15 to 35 mg/ml, are then prepared by diluting this stock solution. The BiI_3 BFs are fabricated through a spin-coating process at 2000 rpm for 35 seconds, conducted at room temperature (~25°C) and under humidity conditions between 60-75%. Additionally, a BiI_3 thin film is prepared using a more

concentrated solution of 100 mg/ml (169.58 mM) and using a modified spinning configuration of 10,000 rpm for 20 seconds.

Using a vapor-assisted conversion approach, BiI_3 transforms into $MA_3Bi_2I_9$. MAI powder is heated to 210°C inside a chamber, and BiI_3 BFs substrates are placed 30 cm away from the MAI powder. The chamber is purged with nitrogen gas at ~5 psi during the deposition of MAI for 120 minutes, ensuring the completion of the solid-state reaction between MAI and BiI_3. Afterward, the chamber is allowed to cool down naturally to room temperature.

Characterization of BiI_3 BFs, $MA_3Bi_2I_9$ BFs, and Thin Film: Morphological characterization uses an optical microscope (OLYMPUS, BX53M, Japan) and field emission scanning electron microscope (ZEISS Sigma-300, Germany). Structural characterization employs an X-ray diffractometer (Rigaku ultima 40kV, 40 mA, Cu Kα radiation, Japan). Thickness measurements are performed with atomic force microscopy (Oxford instruments, U.K.). UV-Vis absorbance and reflectance spectra are collected using a UV-visible spectrophotometer (Agilent, Cary-5000, U.S.). Photoluminescence (PL) study utilizes a HORIBA FluroMAX3 instrument with an excitation wavelength of 425 nm. Raman spectroscopy and X-ray photoelectron spectroscopy measurements are conducted using Jobin-Yvon T64000 and SCIENTA OMICRON SPHERA, respectively. EDS (Energy-dispersive X-ray spectroscopy) measurements are obtained using field emission scanning electron microscopy (JEOL, JSM-7500F, Japan).

Photodetector Device Fabrication and Characterization: Photodetectors are fabricated on etched/patterned ITO-coated glass substrates. The effective active areas of $MA_3Bi_2I_9$ BFs and thin film-based photodetectors measure 2.73×10^{-4} cm^2 and 1.34×10^{-3} cm^2, respectively. For photocurrent measurement, a Lakeshore probe station (Model: TTPS 100, U.S.) is used in conjunction with a source-measure unit (Keithley 2634B, U.S.). The spectral response of the

devices is assessed using a high throughput F4 spectral illumination system (Holmarc-India). Transient photoresponse is carried out by modulating commercially available LEDs connected to a function generator (Scientific Instruments, SM5070).

FDTD Simulations: To analyze the EM field distributions in $MA_3Bi_2I_9$ BFs, 3D FDTD simulations are performed using the Lumerical FDTD Solutions. A realistic 3D model of $MA_3Bi_2I_9$ BFs is reconstructed based on FE-SEM images and imported into the Lumerical with appropriate material properties. Unpolarized light at specific wavelengths (400 and 600 nm) is introduced for the simulations. The electric field distribution analysis employs a combination of perfectly matched layer (PML) absorbing boundary conditions and frequency domain field profile monitors. In the simulations, air is used as the background dielectric medium.

3. Result and discussions

A detailed description of the process for fabricating $MA_3Bi_2I_9$ BFs using the BiI_3 templating method is illustrated in **Figure 1**a-1c. The process begins by dropping a BiI_3 precursor dissolved in THF onto a pristine glass surface, with the ambient humidity at 60% (Figure 1a). The rapid cooling resulting from solvent evaporation leads to the formation of the BFs. This initiates heterogeneous nucleation centers and promotes water adsorption and condensation. [1,31,32] During spin-coating, continuous THF evaporation transforms the BiI_3 precursor into a thin film while leaving behind residual water droplets. Eventually, these droplets evaporate, forming the BiI_3 BFs, as shown in Figure 1b. The dimensions and distribution of the nanopores within these BFs are tailored by varying the precursor concentration and optimizing the spin-coating parameters. Subsequently, as detailed in Figure S1 and the experimental section, the BiI_3 BFs are exposed to MAI vapors. This exposure triggers a selective solid-state reaction, specifically with the BiI_3 BFs, resulting in the fabrication of the $MA_3Bi_2I_9$ BFs, Figure 1c. Therefore, the nature-inspired BFs

method enabled the formation of the BiI_3 template, which in turn plays a crucial role in the fabrication of $MA_3Bi_2I_9$ BFs.

The morphological features of the freshly synthesized BiI_3 and $MA_3Bi_2I_9$ BFs are investigated using optical and electron microscopy, **Figures 1d-1e** and Figure S2. The micrographs reveal a uniform and continuous distribution of nanoporous structures in BiI_3 and $MA_3Bi_2I_9$ BFs. The nanopores are randomly distributed yet distinctly separate, predominantly exhibiting a circular form. The radius of these nanopores typically ranges from 247 to 423 nm, while the mean distance between individual nanopores is around 1.1 μm. BFs exhibit corrugated nanopore edges in BiI_3 in contrast to the smooth edges in $MA_3Bi_2I_9$, Figures 1e and 1f, consistent with polymer BFs elsewhere.[21] Additionally, to demonstrate the versatility of the BFs self-assembly process to various metal halides, SbI_3 BFs were also investigated (Figure S3, Supporting Information). This highlights the flexibility and usability of the nature-inspired BFs technique for other metal halides and inorganic materials.

To evaluate the randomness and dispersity within the nanoporous structure of the BiI_3 BFs, a Voronoi polygon analysis was performed on the FESEM image (Figure 1d). This reveals that the BiI_3 BFs display a polydispersity in the nanopore arrangement, with the number of nearest neighbors for each pore ranging between 3 to 7, as indicated in **Figure 2**a. For each pore, the probabilities of having a specific number of nearest neighbors yielding P_3=0.09, P_4=0.18, P_5=0.42, P_6=0.20, and P_7=0.17, as summarized in Figure 2b and Table-1. Alternatively, the polymer BFs typically exhibit a more uniform mesoporous structure with hexagonal packing (P_6), indicating a monodispersed arrangement.[32] Furthermore, the conformational entropy (S) of the nanopores, calculated using the equation $S=-P_i \sum \ln(P_i)$, revealed values of 1.35 and 0.41 for BiI_3 and polymer BFs, respectively.[32] The higher conformational entropy in BiI_3 BFs is attributed to the

polydispersity of the nanopores. This polydispersity arises from the coagulation and merging of water droplets, which possess high surface curvature during the formation of BiI_3 BFs, owing to the low viscosity of the precursor solution compared to the polymer precursor solution.[9]

The geometric morphology of BiI_3 BFs is tuned by varying the concentration of the precursor, between 15-35 mg/ml. At concentrations below 15 mg/ml, the precursor leads in sparsely distributed mesopores, whereas at concentrations above 35 mg/ml, it forms a uniform thin film. A clear correlation is observed where an increase in precursor concentration corresponds to a decrease in pore size and an increase in pore density, as shown in Figures 2c-2g. The key geometric parameters of the BiI_3 BFs, such as fill factor, pore radius, pore density, and average pore distance, are quantified through a detailed statistical analysis of FESEM micrographs (processed using ImageJ software, Figure S4 in the Supporting Information).[33] These geometric parameters are depicted in Figures 2h-2i and detailed in Supporting Information Table S1. As the precursor concentration is increased from 15 to 35 mg/ml, there is a notable decrease in the pore radius (from 423 to 247 nm) and the average pore distance (from 1.7 to 0.8 μm). A higher concentration of precursor during the BFs formation reduces the effects of evaporative cooling, which limits the growth of water droplets and leads to smaller pores and lower porosity.[9] In contrast, pore density and fill factor progressively increase with the rise in precursor concentration, from 15 to 35 mg/ml (Figure 2g). A higher precursor concentration reduces the temperature gradient at the solution interface, which minimizes water condensation and inhibits water droplet coalescence, resulting in a higher fill factor and average pore distance. Therefore, BiI_3 BFs provide an adaptable approach to tailor the size and distribution of nanopores precisely by adjusting the precursor concentration.

The potential of the BiI_3 BFs template is explored by transforming it to halide perovskite BFs. Using a 20 mg/ml BiI_3 precursor solution, BiI_3 BFs are fabricated and then exposed to MAI vapor, forming perovskite-inspired $MA_3Bi_2I_9$ BFs. This specific concentration is crucial for successfully transforming $MA_3Bi_2I_9$ BFs, offering an optimal combination of porosity, pore density, and uniform pore size (Figure S5, Supporting Information). Note that BiI_3 BFs fabricated with concentrations exceeding 20 mg/ml tend to form smaller pores (~ 260 nm), which essentially seal off the nano-porosity during the conversion to $MA_3Bi_2I_9$. On the other hand, BFs fabricated with concentrations less than 15 mg/ml of BiI_3 show irregular pore sizes and reduced pore density, making them less suitable for this conversion. The X-ray diffraction (XRD) patterns presented in **Figure 3**a validate the existence of BiI_3 and confirm the synthesis of perovskite-inspired $MA_3Bi_2I_9$. The reflexes in the XRD pattern correspond to the orthorhombic phase of BiI_3 BFs, transforming into the hexagonal phase (space group $P6_3/mmc$) of $MA_3Bi_2I_9$ after MAI vapor exposure.[34–36] This is indicated by a downward shift in the (006) peak and disappearance of precursor (MAI and BiI_3) material reflections. The $MA_3Bi_2I_9$ BFs, compared to pristine BiI_3 BFs, exhibit smaller nanopores and reduced grain size, Figure S6. The AFM image in Figure S7 shows an increased thickness for $MA_3Bi_2I_9$ BFs (254 nm) compared to BiI_3 BFs (180 nm), suggesting the integration of MAI molecules.

Geometric parameters of BiI_3 BFs and the corresponding $MA_3Bi_2I_9$ BFs are presented in the histograms shown in Figure 3b. $MA_3Bi_2I_9$ BFs show an increase in the thickness (Δt = 74 nm) and fill factor (ΔFF = 3.7%) but a decrease in average pore radius (from 369 to 260 nm). Even after transformation, the average pore distance remains consistent, Figure 3c, indicating the robustness of the BiI_3 BFs template under MAI vapor exposure. Additionally, smoother pore edges in $MA_3Bi_2I_9$ BFs are observed in Figures S6b and S6c, attributed to volume expansion and grain

size increase. The presence of specific bonding states of carbon I, nitrogen (N), iodine (I), and bismuth (Bi) in $MA_3Bi_2I_9$ BFs are confirmed by EDS mapping and XPS spectra (Figures S8 and S9).[37,38] A shift in the valence band spectra is observed, from 1.14 eV (BiI_3) to 1.35 eV ($MA_3Bi_2I_9$), Figure S9f, indicating a change in the band structure.[37] The Raman spectrum of $MA_3Bi_2I_9$ BFs, Figure S10a, displays peaks at 109 and 144 cm^{-1}, corresponding to Bi-I stretching modes of $[BiI_6]^{3-}$.[39] Therefore, the XRD, XPS, EDS, and Raman spectra confirm the formation of perovskite-inspired $MA_3Bi_2I_9$ BFs.

The optical properties of $MA_3Bi_2I_9$ BFs are compared to a $MA_3Bi_2I_9$ thin film, with absorption spectra indicating different band gaps of 2.07 eV and 2.19 eV for $MA_3Bi_2I_9$ BFs and thin film, respectively (Figure S10b and S10c, Supporting Information).[40] The extinction coefficient (k) for $MA_3Bi_2I_9$ BFs and thin film is determined using the following equation 1.[41]

$$k = \frac{\alpha\lambda}{4\pi} \text{ where, } \alpha = \frac{1}{d}\ln\left[\frac{(1-R)^2}{2T} + \sqrt{\frac{(1-R)^4}{4T^2} + R^2}\right] \quad (1)$$

Here, T, R, d, and α denote transmittance, reflectance, thickness, and absorption coefficient, respectively. The extinction spectra reveal a characteristic exciton peak at 507 nm for $MA_3Bi_2I_9$ BFs and thin film (see **Figure 4**a). The extinction coefficients for $MA_3Bi_2I_9$ BFs (0.3) and thin film (0.22) are comparable to reported values, such as 0.15 for $MA_3Bi_2I_9$ and 0.5 for $MAPbI_3$ at the same wavelength of 510 nm.[39,42,43] Notably, $MA_3Bi_2I_9$ BFs exhibit enhanced extinction compared to the thin film, owing to multiple scattering and photon reabsorption.[25] The high surface-to-volume ratio of $MA_3Bi_2I_9$ BFs contributes to superior light absorption, enhancing overall light harvesting. Photoluminescence (PL) analysis in Figure 4a demonstrates a narrower emission spectrum and a blue shift (of 13 nm) for $MA_3Bi_2I_9$ BFs, compared to the thin film, suggesting a reduced trap density and photon reabsorption at the nanopores. Furthermore, the observed blue shift (of 13 nm) and narrower PL emission in $MA_3Bi_2I_9$ BFs are attributed to the

absence of self-trap emission (STE) and the enhancement of direct emission (see Figure S11a-b), both of which are crucial for optoelectronic devices.[29,44,45] The refractive index is measured through spectral reflectance using the formula $n = \frac{1+\sqrt{R}}{1-\sqrt{R}}$ where n>>k[41] is lower in $MA_3Bi_2I_9$ BFs in the 300-600 nm wavelength range (Figure 4b), which is attributed to a higher air volume fraction in nanopores. This is in contrast to the thin film (Figure S10d), which shows interference fringes due to light reflection at the top and bottom surfaces of the thin film. An abrupt change in refractive index near 650 nm in $MA_3Bi_2I_9$ BFs is due to strong optical scattering at nanopores.

3D-FDTD simulations are performed using a reconstructed model of the $MA_3Bi_2I_9$ BFs unit cell (Figure S12). **Figures 5**a-5d depict the simulated electric field distribution for $MA_3Bi_2I_9$ BFs, closely emulating their optical properties. Notably, EM radiation with a 400 nm wavelength exhibits a significantly enhanced electric field compared to a 600 nm wavelength. With nanopores measuring 269 nm in size in $MA_3Bi_2I_9$ BFs, the 400 nm wavelength light is reflected off the walls of the nanopores and confined at their centers, Figure 5b.[46] In the case of the 600 nm wavelength, as depicted in Figures 5c and d, the observed light confinement within the pores suggests the potential for light-matter interaction beyond the band gap of $MA_3Bi_2I_9$ BFs. The results of the 3D-FDTD simulations emphasize the wavelength-dependent confinement behavior of light within the nanoporous $MA_3Bi_2I_9$ BFs, emphasizing the crucial interplay between nanopore size and incident wavelength in determining the EM field distribution.[46]

The potential of $MA_3Bi_2I_9$ BFs for optoelectric applications is investigated by fabricating a photodetector on a patterned ITO-coated substrate (Figure S13). The photocurrent response of the detector is tested under varying white light intensities (ranging from 1.6 to 3310 $\mu W/cm^2$) and a voltage sweep from -1 to 1V, **Figure 6**a. The device exhibits consistent photoresponse even at low light intensities (1.6 $\mu W/cm^2$). The spectral responsivity ($R_\lambda = I_{ph}/P_{in}$), which is defined as the

photocurrent density (I_{ph}) per unit light intensity (P_{in}), is plotted in Figure 6b for $MA_3Bi_2I_9$ BFs and thin film photodetectors.[47] $MA_3Bi_2I_9$ BFs exhibit the highest R_λ value of 0.44 A/W at 400 nm, significantly outperforming the thin film counterpart by three orders of magnitude. This enhanced performance spans a broad spectral range from 400 to 740 nm, indicating $MA_3Bi_2I_9$ BFs enhanced light detection capability. In terms of broadband detectivity ($D_\lambda = (R_\lambda/2qJ_d)^{1/2}$), the $MA_3Bi_2I_9$ BFs-based photodetector demonstrates a highest value of 1.28×10^{12} Jones (Figure 6c).[47] Additionally, the external quantum efficiency (EQE) of $MA_3Bi_2I_9$ BFs, analogous to R_λ and D_λ, has a maximum value of 132% at 400 nm (Figure 6c), consistent with the electric field enhancement observed in the FDTD simulations (Figure 5a-5d).[48] High EQE values positively correlate with the extraction of carriers under light illumination while inversely relating to injecting photon-excited carriers into trap states.[49] The linear dynamic range (LDR) of the $MA_3Bi_2I_9$ BFs-based photodetector achieves a significant value of 62.4 dB (Figure S14). This improved performance is ascribed to the multiple scattering of photons trapped near the nanopores, consistent with the increased extinction coefficients (Figure 4a) and supported by the findings from FDTD simulations (Figure 5a-5d). The response time of the photodetector is determined by fitting exponential rise and decay curves to a single on/off cycle at a frequency of 0.25 Hz, revealing rise (τ_{res}) and fall (τ_{rec}) times of 145 and 180 ms, respectively (Figure S15). The photodetector demonstrated excellent durability by consistent photocurrent response over 1150 switching cycles and maintained a stable photoresponse for five weeks under atmospheric conditions, highlighting the light-soaking and environmental stability of $MA_3Bi_2I_9$ BFs (see Figure S16). These results highlight the practicality and reliability of the $MA_3Bi_2I_9$ BFs-based photodetector for various optoelectronic applications. **Figure 7**a depicts the photocurrent (I_{ph}) and responsivity (*R)* under various white light intensities. The photocurrent follows a sublinear relationship, fitting the power

equation, $I_{ph}\ \alpha\ P_{in}^{\alpha}$, where α = 0.35. This sublinearity is attributed to surface traps within the device.[50] Moreover, the $MA_3Bi_2I_9$ thin films demonstrated a power exponent value one order less than BFs (see Figure S17), indicating the presence of sub-bandgap trap states consistent with PL spectra. The responsivity of the $MA_3Bi_2I_9$ BFs photodetector reaches up to 1.01 A/W under a white light intensity of 1.6 μW/cm^2. Compared to solution-processed $A_3B_2I_9$ (A=Cs, MA, and B=Bi, Sb) thin film-based photodetectors (Figure 7b and Table S3), the $MA_3Bi_2I_9$ BFs exhibit a remarkably higher responsivity and detectivity.[39,51–59] This sets a new standard for photoresponse performance among thin film $A_3B_2I_9$-based photodetectors.

4. Conclusions

This work presents a solution-based and nature-inspired BFs approach to fabricate halide perovskite nanoporous thin films. By adjusting the BiI_3 precursor concentration, precise control over the geometric features of the BiI_3 BFs is obtained (varying the nanopore radius from 423 to 247 nm). Unlike polymer BFs, BiI_3 BFs exhibit a polydisperse nanopore structure with higher conformational entropy. The BiI_3 BFs act as templates that, undergoing a solid-state reaction with MAI vapors, are transformed into halide perovskite $MA_3Bi_2I_9$ BFs. The resultant $MA_3Bi_2I_9$ BFs exhibit enhanced light extinction and a lower refractive index than their thin film counterparts, which is due to the increased air volume fraction within the nanopores. Additionally, 3D-FDTD simulations reveal that light confinement within the $MA_3Bi_2I_9$ BFs, facilitates electric field distribution. The fabricated photodetector based on $MA_3Bi_2I_9$ BFs exhibits three orders of magnitude higher responsivity than their thin-film counterpart, with a responsivity reaching up to 1 A/W, significantly surpasses that of solution-processed $A_3B_2I_9$ thin film photodetectors. This enhanced performance is primarily due to the multiple scattering of photons trapped near the nanopores. Inspired by natural dewetting phenomenon, the BFs method enables complex

nanopatterning across various halide perovskites, offering a precise control over light-matter interactions, laying the groundwork for cutting-edge advancements in optoelectronics.

Supporting Information

Supporting Information is available from the Wiley Online Library or from the author.

ACKNOWLEDGMENT

P. Sarkar acknowledges CSIR-UGC for fellowship and IACS for research facilities. K. D. M. R. acknowledges the financial support from the Science and Engineering Research Board (SERB) project CRG/2022/004873 and also acknowledges support from the Technical Research Center (TRC, Project No. AI/I/65/IACS/2014G), IACS, Kolkata. M.C. acknowledges the financial support from the Novo Nordisk Foundation under the grant Nanoscale Energy Generators (number NNF20OC0064735).

Conflicts of Interest

There are no conflicts to declare.

References

[1] M. Srinivasarao, D. Collings, A. Philips, S. Patel, *Science* **2001**, *292*, 79.
[2] L. Song, R. K. Bly, J. N. Wilson, S. Bakbak, J. O. Park, M. Srinivasarao, U. H. F. Bunz, *Adv. Mater.* **2004**, *16*, 115.
[3] B. W. Lim, M. C. Suh, *Nanoscale* **2014**, *6*, 14446.
[4] F. Galeotti, W. Mróz, G. Scavia, C. Botta, *Org. Electron.* **2013**, *14*, 212.
[5] H. Tang, J. P. Tu, X. Y. Liu, Y. J. Zhang, S. Huang, W. Z. Li, X. L. Wang, C. D. Gu, *J. Mater. Chem. A* **2014**, *2*, 5834.
[6] C. Wang, Q. Liu, X. Shao, G. Yang, H. Xue, X. Hu, *Talanta* **2007**, *71*, 178.
[7] J. Liang, Y. Ma, S. Sims, L. Wu, *J. Mater. Chem. B* **2015**, *3*, 1281.
[8] T. J. Baker, *London, Edinburgh, Dublin Philos. Mag. J. Sci.* **1922**, *44*, 752.
[9] A. Zhang, H. Bai, L. Li, *Chem. Rev.* **2015**, *115*, 9801.
[10] Washizu, S.; Yamazaki, H.; Yamanouchi, J.; Naruse, H. EP Patent 20,060,010,988, **2012**.
[11] D. Ji, T. Li, H. Fuchs, *Nano Today* **2020**, *31*, 100843.
[12] R. Cheng, R. N. P. Colombo, L. Zhang, D. H. T. Nguyen, R. Tilley, S. I. Cordoba de Torresi,

L. Dai, J. J. Gooding, V. R. Gonçales, *ACS Appl. Mater. Interfaces* **2020**, *12*, 55181.
[13] P. Escalé, L. Rubatat, L. Billon, M. Save, *Eur. Polym. J.* **2012**, *48*, 1001.
[14] F. Galeotti, W. Mróz, A. Bolognesi, *Soft Matter* **2011**, *7*, 3832.
[15] Y. Dou, M. Jin, G. Zhou, L. Shui, *Membranes* **2015**, *5*, 399.
[16] J. Rodríguez-hernández, E. Bormashenko, Breath Figures Mechanisms of Multi-Scale Patterning and Strategies for Fabrication and Applications of Microstructured Functional Porous Surfaces, Springers**, 2020.**
[17] R. Xing, Z. Li, W. Zhao, D. Wang, R. Xie, Y. Chen, L. Wu, X. Fang, *Adv. Mater.* **2024**, *36*, 2310248.
[18] X. Zhang, Z. Li, E. Hong, M. Deng, L. Su, X. Fang, *Adv. Funct. Mater.* **2023**, *2312293*.
[19] S. Li, X. Liu, H. Yang, H. Zhu, X. Fang, *Nat. Electron.* **2024**, *7*, 216.
[20] F. Cao, T. Yan, Z. Li, L. Wu, X. Fang, *Adv. Opt. Mater.* **2022**, *10*, 2200786.
[21] X. Zhang, B. Wang, L. Huang, W. Huang, Z. Wang, W. Zhu, Y. Chen, Y. Mao, A. Facchetti, T. J. Marks, *Sci. Adv.* **2020**, *6*, eaaz1042.
[22] Y. Ou, L. W. Zhu, W. Da Xiao, H. C. Yang, Q. J. Jiang, X. Li, J. G. Lu, L. S. Wan, Z. K. Xu, *J. Phys. Chem. C* **2014**, *118*, 4403.
[23] J. Wang, C. F. Wang, H. X. Shen, S. Chen, *Chem. Commun.* **2010**, *46*, 7376.
[24] H. Zhao, Y. Shen, S. Zhang, H. Zhang, *Langmuir* **2009**, *25*, 11032.
[25] J. Xue, Y. Gu, Q. Shan, Y. Zou, J. Song, L. Xu, Y. Dong, J. Li, H. Zeng, *Angew. Chemie - Int. Ed.* **2017**, *56*, 5232.
[26] M. Kanatzidis, H. Sun, S. Dehnen, *Inorg. Chem.* **2020**, *59*, 3341.
[27] R. E. Brandt, V. Stevanović, D. S. Ginley, T. Buonassisi, *MRS Commun.* **2015**, *5*, 265.
[28] X. Zheng, W. Zhao, P. Wang, H. Tan, M. I. Saidaminov, S. Tie, L. Chen, Y. Peng, J. Long, W. H. Zhang, *J. Energy Chem.* **2020**, *49*, 299.
[29] S. Sun, M. Lu, X. Gao, Z. Shi, X. Bai, W. W. Yu, Y. Zhang, *Adv. Sci.* **2021**, *8*, 2102689.
[30] C. McDonald, C. Ni, V. Švrček, M. Lozac'H, P. A. Connor, P. Maguire, J. T. S. Irvine, D. Mariotti, *Nanoscale* **2017**, *9*, 18759.
[31] M. S. Park, J. K. Kim, *Langmuir* **2004**, *20*, 5347.
[32] U. H. F. Bunz, *Adv. Mater.* **2006**, *18*, 973.
[33] M. D. Abràmoff, P. J. Magalhães, S. J. Ram, in *Opt. Imaging Tech. Cell Biol.*, CRC Press, **2006**, 249.
[34] K. Eckhardt, V. Bon, J. Getzschmann, J. Grothe, F. M. Wisser, S. Kaskel, *Chem. Commun.* **2016**, *52*, 3058.
[35] V. Vuong, S. V. N. Pammi, K. S. Pasupuleti, W. Hu, V. D. Tran, J. S. Jung, M. Kim, V. Pecunia, S. G. Yoon, *Adv. Opt. Mater.* **2021**, *9*, 2100192.
[36] P. Chang, C. Li, F. Fu, K. Huang, A. Chou, C. Wu, *Adv. Funct. Mater.* **2018**, *28*, 1800179.
[37] S. M. Jain, D. Phuyal, M. L. Davies, M. Li, B. Philippe, C. De Castro, Z. Qiu, J. Kim, T. Watson, W. C. Tsoi, O. Karis, H. Rensmo, G. Boschloo, T. Edvinsson, J. R. Durrant, *Nano Energy* **2018**, *49*, 614.
[38] V. H. Vuong, S. V. N. Pammi, S. Ippili, V. Jella, T. Nguyen Thi, K. Sairam Pasupuleti, M.

D. Kim, M. Ji Jeong, J. R. Jeong, H. Sik Chang, S. G. Yoon, *Chem. Eng. J.* **2023**, *458*, 141473.
[39] S. Shah, A. Bhorde, Y. Hase, R. Aher, V. Doiphode, A. Waghmare, A. Punde, P. Shinde, S. Rahane, B. R. Bade, H. M. Pathan, M. Prasad, M. Aleksandrova, S. P. Patole, S. R. Jadkar, *ACS Appl. Electron. Mater.* **2022**, *4*, 2793.
[40] S. Valastro, S. Gavranovic, I. Deretzis, M. Vala, E. Smecca, A. La Magna, A. Alberti, K. Castkova, G. Mannino, *Adv. Opt. Mater.* **2023**, *2302397*.
[41] Jacques I. Pankove, Optical Processes In Semiconductors, Dover Publications, Inc. New York, **1971.**
[42] Y. Jiang, M. A. Green, R. Sheng, A. Ho-Baillie, *Sol. Energy Mater. Sol. Cells* **2015**, *137*, 253.
[43] P. Löper, M. Stuckelberger, B. Niesen, J. Werner, M. Filipič, S.-J. Moon, J.-H. Yum, M. Topič, S. De Wolf, C. Ballif, *J. Phys. Chem. Lett.* **2015**, *6*, 66.
[44] Y. Zhang, J. Yin, M. R. Parida, G. H. Ahmed, J. Pan, O. M. Bakr, J.-L. Brédas, O. F. Mohammed, *J. Phys. Chem. Lett.* **2017**, *8*, 3173.
[45] V. Sarritzu, N. Sestu, D. Marongiu, X. Chang, Q. Wang, S. Masi, S. Colella, A. Rizzo, A. Gocalinska, E. Pelucchi, M. L. Mercuri, F. Quochi, M. Saba, A. Mura, G. Bongiovanni, *Adv. Opt. Mater.* **2018**, *6*, 1701254.
[46] M. Li, K. Shen, H. Xu, A. Ren, J. Lee, S. Kunwar, S. Liu, J. Wu, *Small* **2020**, *16*, 2004234.
[47] M. Hossain, G. S. Kumar, S. N. Barimar Prabhava, E. D. Sheerin, D. McCloskey, S. Acharya, K. D. M. Rao, J. J. Boland, *ACS Nano* **2018**, *12*, 4727.
[48] K. D. M. Rao, M. Hossain, Umesh, A. Roy, A. Ghosh, G. S. Kumar, P. Moitra, T. Kamilya, S. Acharya, S. Bhattacharya, *Nanoscale* **2020**, *12*, 11986.
[49] Z. Yang, Y. Deng, X. Zhang, S. Wang, H. Chen, S. Yang, J. Khurgin, N. X. Fang, X. Zhang, R. Ma, *Adv. Mater.* **2018**, *30*, 1704333.
[50] Y. Li, S. Wang, J. Hong, N. Zhang, X. Wei, T. Zhu, Y. Zhang, Z. Xu, K. Liu, M. Jiang, H. Xu, *Small* **2023**, *19*, 2302623.
[51] A. Popoola, M. A. Gondal, L. E. Oloore, I. K. Popoola, *ACS Appl. Electron. Mater.* **2020**, *2*, 1145.
[52] A. Bhorde, S. Nair, H. Borate, S. Pandharkar, R. Aher, A. Punde, A. Waghmare, P. Shinde, P. Vairale, R. Waykar, V. Doiphode, V. Jadkar, Y. Hase, S. Rondiya, N. Patil, M. Prasad, S. Jadkar, *New J. Chem.* **2020**, *44*, 11282.
[53] W. Li, X. Wang, J. Liao, Y. Jiang, D. Kuang, *Adv. Funct. Mater.* **2020**, *30*, 1909701.
[54] A. A. Hussain, *ACS Appl. Mater. Interfaces* **2020**, *12*, 46317.
[55] S. Devasia, S. Shaji, D. A. Avellaneda, J. A. Aguilar Martinez, B. Krishnan, *Mater. Chem. Phys.* **2023**, *296*, 127295.
[56] Z. Li, X. Liu, C. Zuo, W. Yang, X. Fang, *Adv. Mater.* **2021**, *33*, 2103010.
[57] H. Geng, X. Yao, X. Tu, Z. Wang, Y. Gu, H. Cui, G. Guan, M. Han, *ACS Appl. Electron. Mater.* **2022**, *4*, 217.
[58] S. K. Shil, F. Wang, K. O. Egbo, Y. Wang, C. K. G. Kwok, S.-W. Tsang, J. C. Ho, K. M. Yu, *J. Mater. Chem. C* **2023**, *11*, 4603.

[59] Z. Lai, Y. Meng, F. Wang, X. Bu, W. Wang, P. Xie, W. Wang, C. Liu, S. P. Yip, J. C. Ho, *Nano Res.* **2022**, *15*, 3621.

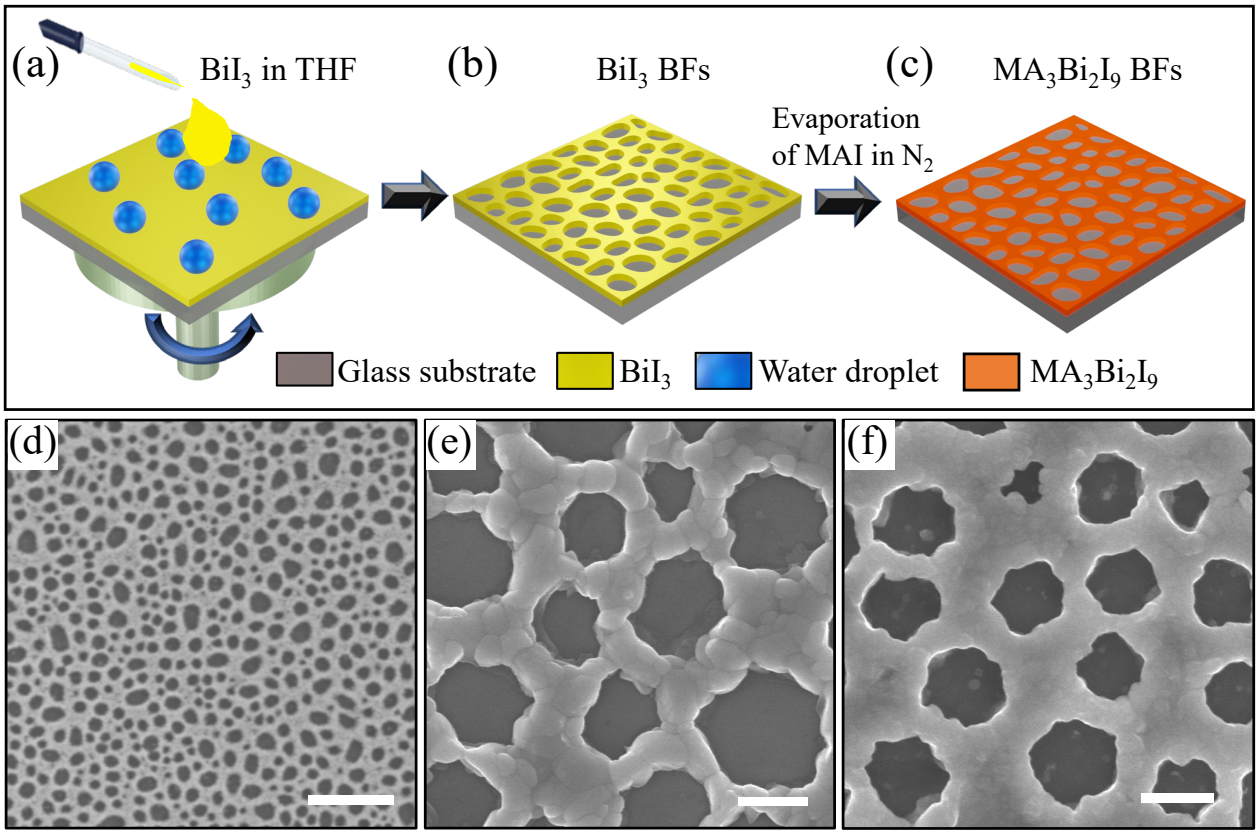

Figure 1: Illustration depicting the fabrication process of $MA_3Bi_2I_9$ Breath Figures (BFs). (a) Application of BiI_3 solution via spin-coating on a substrate induces water droplet condensation at interfaces, (b) leading to the formation of BiI_3 BFs. (c) MAI evaporation in an inert N_2 atmosphere is employed for $MA_3Bi_2I_9$ BFs fabrication. FESEM micrographs of BiI_3 BFs at different magnifications (d)-(e), and magnified view of the converted $MA_3Bi_2I_9$ BFs (c). (Scale bars denoted as (d) 5 µm, (e) and (f) 500 nm).

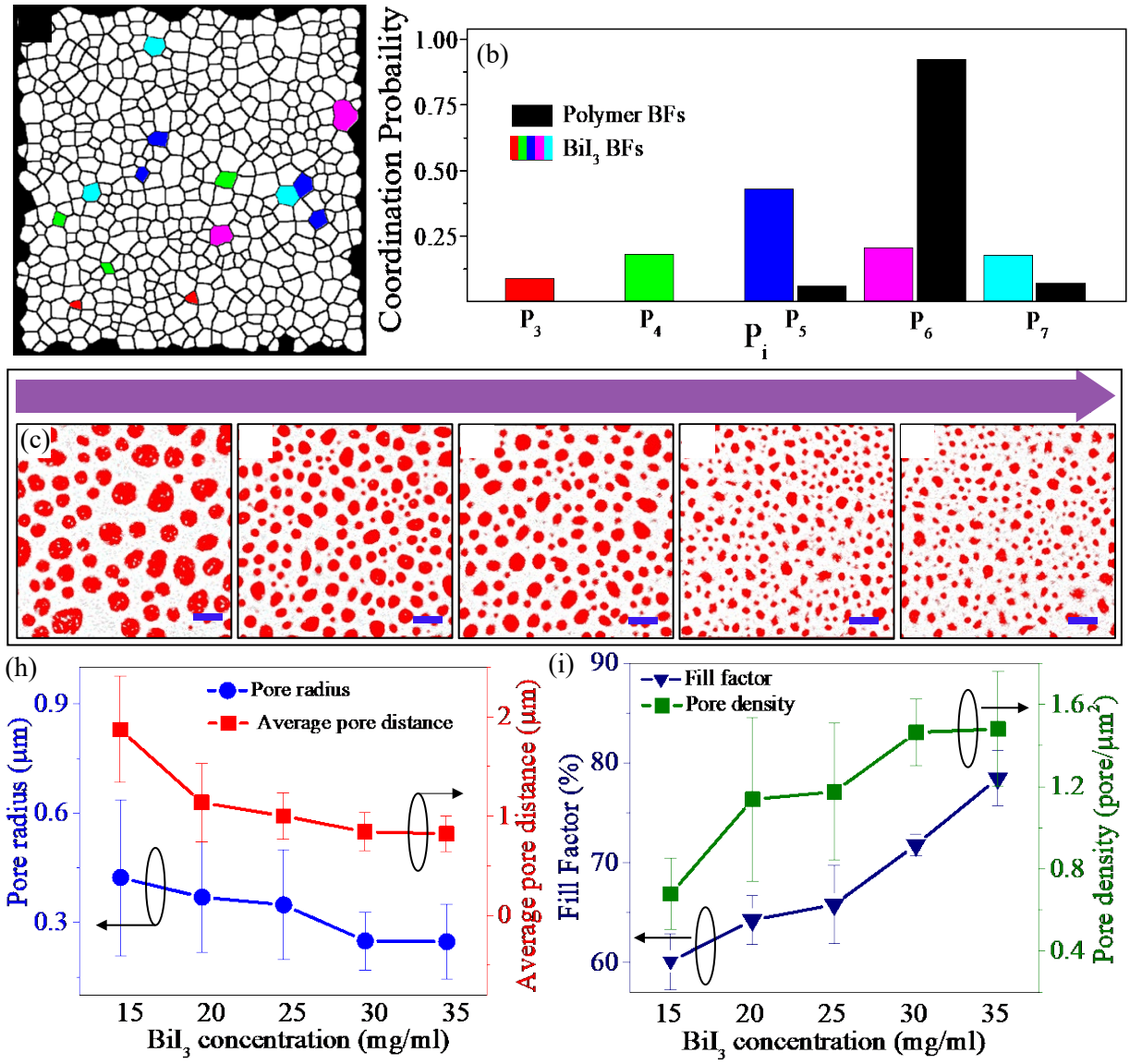

Figure 2: (a) Voronoi polygon analysis of BiI_3 BFs in (figure1d), and (b) corresponding coordination probabilities for polygons with three sides (P_3), four sides (P_4), five sides (P_5), six sides (P_6), and seven sides (P_7) presented as a colored histogram, compared with polymer BFs data from literature (black histogram). (c)-(g) FESEM micrographs (flase colored) illustrating BiI_3 BFs at varying BiI_3 precursor concentrations (15 to 35 mg/ml), with a scale bar of 2 μm. (h) Graph depicting pore size and pore-to-pore distance, and (i) graph illustrating porosity and pore density for distinct concentrations of BiI_3.

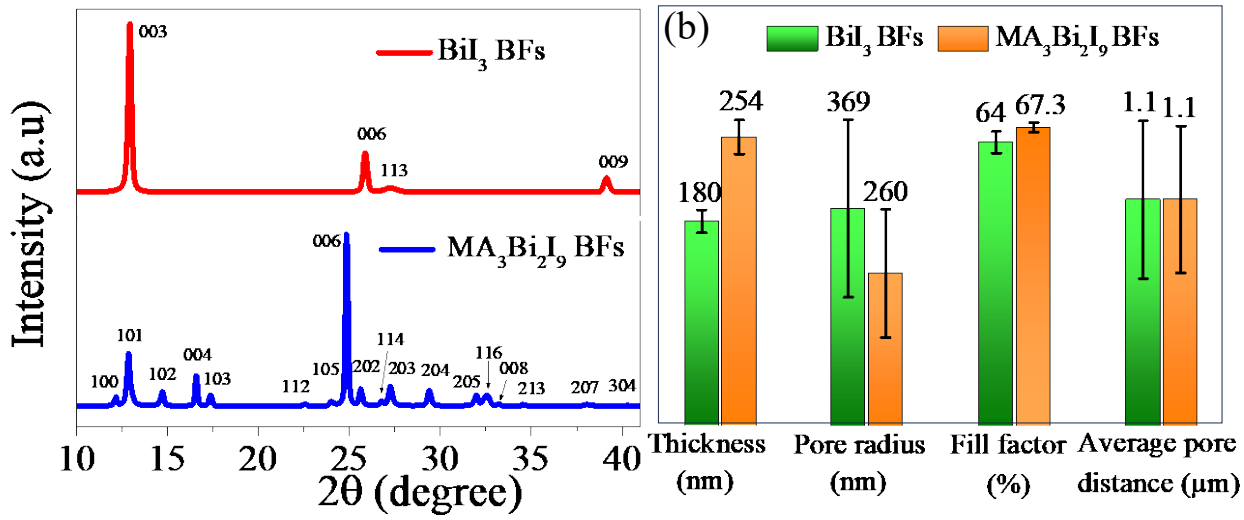

Figure 3: (a) X-ray diffraction patterns of BiI_3 BFs in red and $MA_3Bi_2I_9$ BFs in blue. (b) Comparative statistical analysis of thickness, pore radius, fill factor, and average pore distance between BiI_3 BFs and $MA_3Bi_2I_9$ BFs.

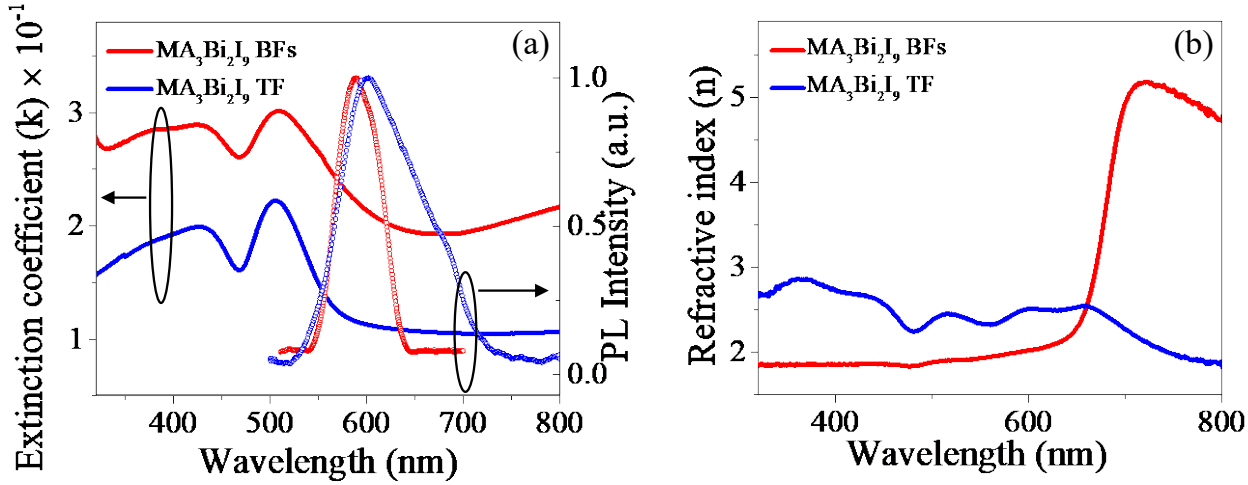

Figure 4: (a) Optical extinction spectra (solid line) and Photoluminescence (PL) spectra (scatter point) of $MA_3Bi_2I_9$ BFs and thin film at room temperature, (b) wavelength-dependent variation of the refractive index for the $MA_3Bi_2I_9$ BFs and thin film. The $MA_3Bi_2I_9$ BFs and thin film data are represented in red and blue colors.

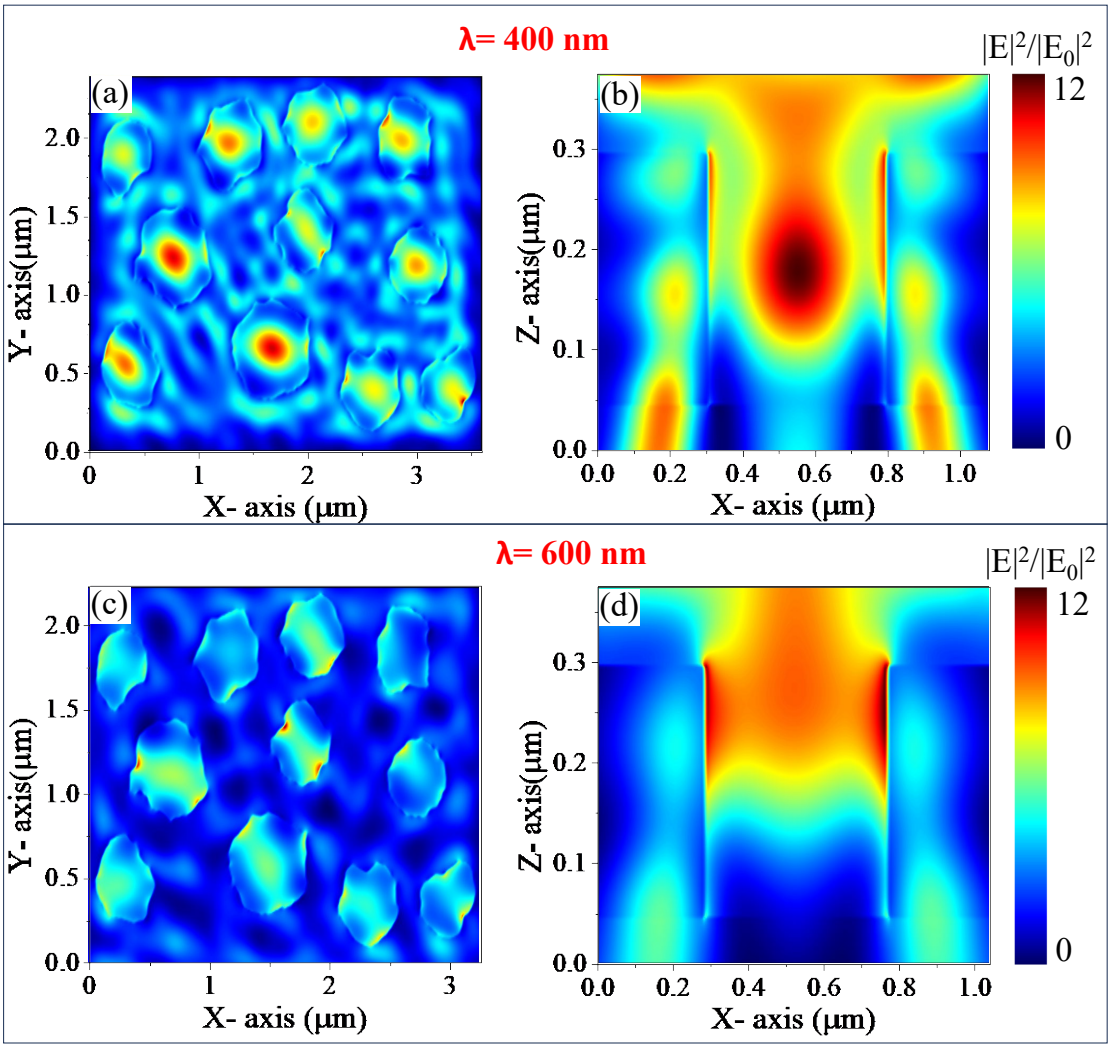

Figure 5: FDTD simulation illustrating the electromagnetic (EM) field distribution (top view) of $MA_3Bi_2I_9$ BFs under illumination with (a) 400 nm and (c) 600 nm peak wavelengths. Corresponding cross-sectional EM distribution within a single pore for the (b) 400 nm and (d) 600 nm wavelength. The propagation direction of light is in the Z direction.

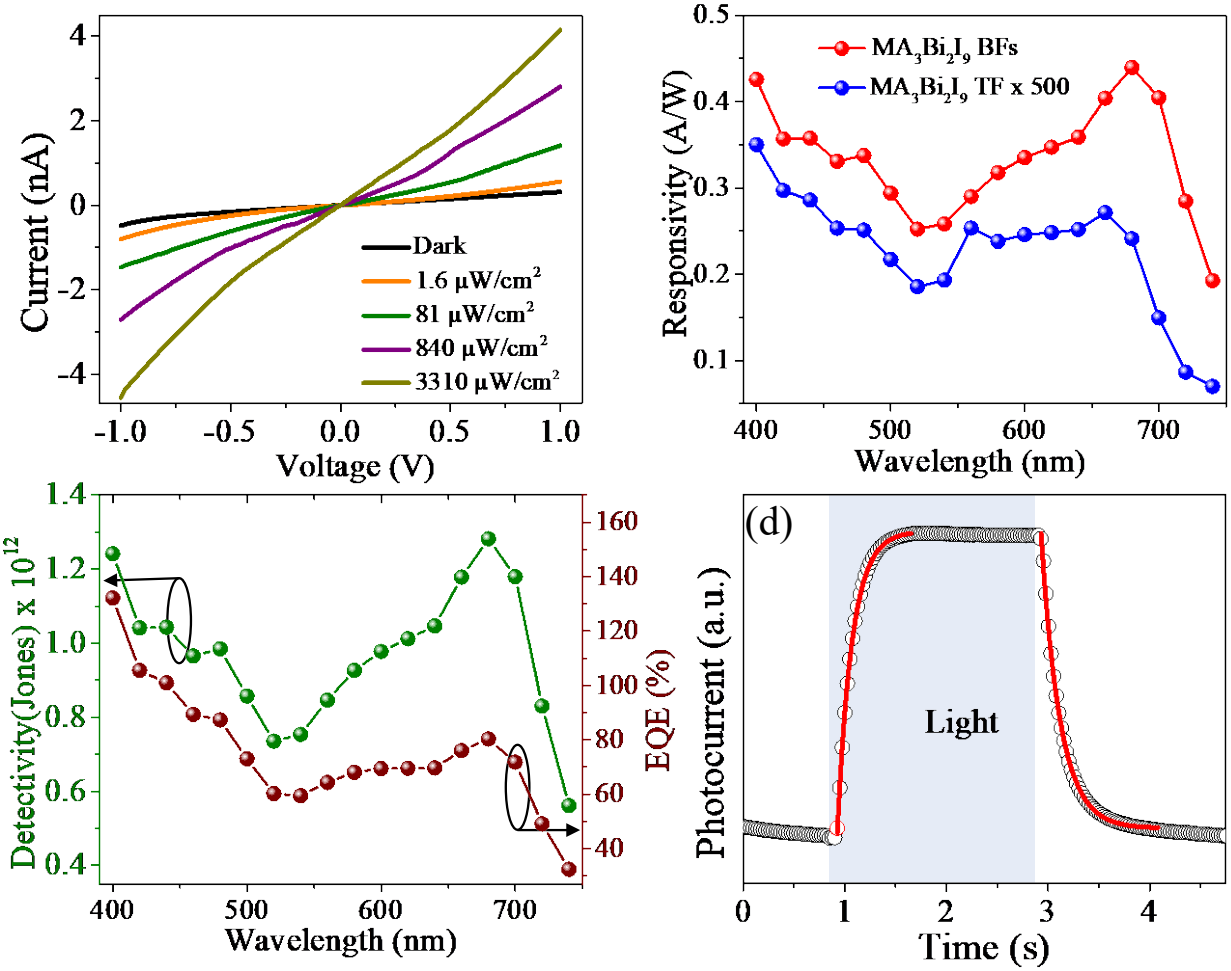

Figure 6: $MA_3Bi_2I_9$ BFs-based photodetector, (a) Photocurrent at different white light intensities as a function under applied voltage sweep from -1 to 1 V. (b) Comparison of the spectral responsivity plot between $MA_3Bi_2I_9$ BFs and thin film-based devices. (c) Plot of detectivity and external quantum efficiency (EQE) for the $MA_3Bi_2I_9$ BFs. (d) Calculation of rise and fall times using exponential fit.

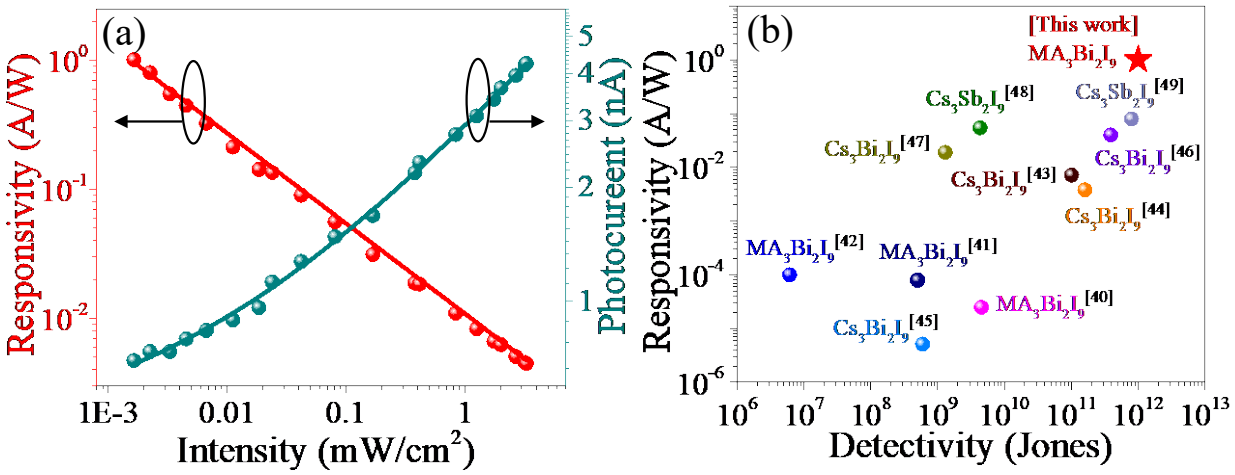

Figure 7: (a) Responsivity and photocurrent as functions of light intensity for the $MA_3Bi_2I_9$ BFs extracted from (figure1d). (b) Comparison of responsivity and detectivity with solution-processed $A_3B_2I_9$ (A= MA, Cs, and B=Bi, Sb) thin film-based photodetectors.

Table 1: The Voronoi polygon analysis of BiI_3 BFs (Total number of polygons is 464)

S. No.	Number of nearest neighbors	Number of polygons	Probability of polygon P_i	ln P_i	$S=-P_i \sum \ln P_i$
1.	3	4	0.009	-4.710	1.346
2.	4	84	0.181	-1.709	
3.	5	199	0.429	-0.846	
4.	6	95	0.205	-1.585	
5.	7	82	0.177	-1.732	

Table 2: Comparison of photodetector performance for the $MA_3Bi_2I_9$ RNT and thin film-based devices.

S. No.	Surface type	*R (A/W)	*D (Jones)	EQE (%)	τ_r and τ_f (ms)	LDR (dB)
1.	$MA_3Bi_2I_9$ BFs	1.01	1.28×10^{12}	132	145 and 180	62.43
2.	$MA_3Bi_2I_9$ Thin Film	7.0×10^{-4}	7.54×10^{9}	0.217	170 and 182	36.62

*R: responsivity, *D: detectivity

Table of Content